

## High Frequency MoS<sub>2</sub> Nanomechanical Resonators

Jaesung Lee<sup>1†</sup>, Zenghui Wang<sup>1†</sup>, Keliang He<sup>2</sup>, Jie Shan<sup>2</sup>, Philip X.-L. Feng<sup>1,\*</sup>

<sup>1</sup>*Department of Electrical Engineering & Computer Science, Case Western Reserve University,  
10900 Euclid Avenue, Cleveland, OH 44106, USA*

<sup>2</sup>*Department of Physics, Case Western Reserve University,  
10900 Euclid Avenue, Cleveland, OH 44106, USA*

### Table of Contents

<b>S1. Measurement of Nanomechanical Resonances</b>	2
<i>S1.1. Optical Interferometry Measurement System</i>	2
<i>S1.2. Interferometric Motion Transduction</i>	4
<i>S1.3. Thermomechanical Resonance Measurement and Noise Analysis</i>	6
<i>S1.4. Calculation of the Effective Mass of the Resonator</i>	9
<i>S1.5. Effect of Device Thickness</i>	10
<b>S2. AFM and Thickness Measurement</b>	11
<b>S3. Theoretical Analysis of Device Elastic Behavior and Frequency Scaling</b>	12
<b>S4. Measuring Device Temperature and Laser Heating Effect</b>	14
<b>S5. Measurement of Pressure Dependence</b>	16
<b>S6. List of All Devices and Their Parameters</b>	18

---

\*Corresponding Author. Email: philip.feng@case.edu. †Equally contributed authors.

## S1. Measurement of Nanomechanical Resonances

### S1.1. Optical Interferometry Measurement System

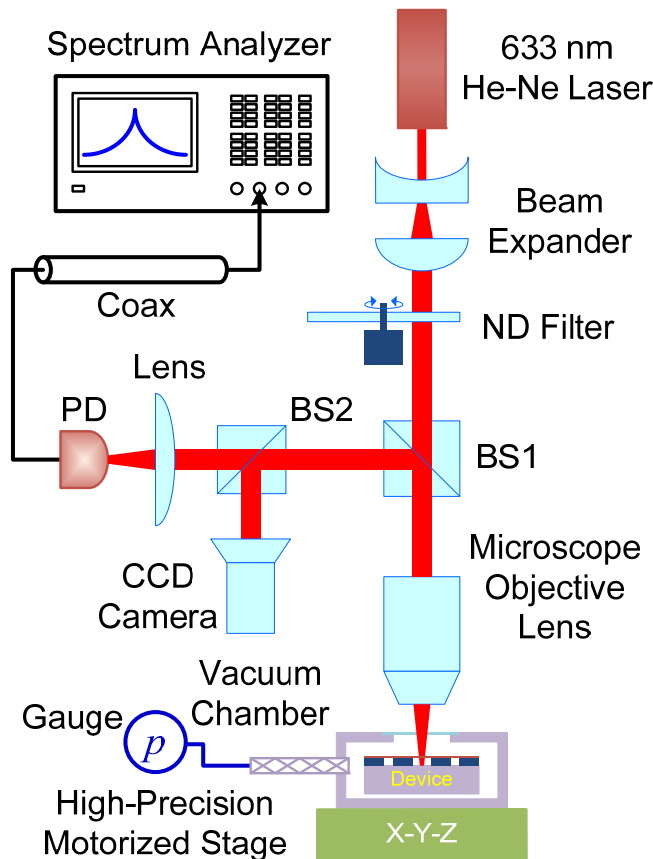


**Figure S1. Schematic of the optical interferometry measurement system.** The 632.8 nm beam from a He-Ne laser goes through a beam expander, followed by a neutral density (ND) filter. It is then focused onto the device through a 50 $\times$  objective with window correction. The reflected beam, redirected by a beam splitter (BS1), is focused onto a photodetector (PD). The electronic signal is transmitted to a spectrum analyzer using a coaxial cable. The second beam splitter (BS2) and the CCD camera facilitate white light imaging. The device operates inside a vacuum chamber with a quartz window.

Figure S1 shows a schematic of the measurement system. Detection of the thermomechanical motion of the MoS<sub>2</sub> devices is based on optical interference from light waves reflected from the suspended MoS<sub>2</sub> diaphragm-vacuum interfaces, and from the vacuum-Si interface (described and

analyzed in more detail in Section S1.2). In this geometry, reflectivity of the bottom Si surface in the microtrench is important for achieving a large interferometry signal. Using buffered oxide etch (BOE) to remove the SiO<sub>2</sub> layer above, we obtain a smooth Si surface that is important for the interferometry. At the laser wavelength 632.8nm, the reflectivity of the Si surface is ~35%.

To achieve a tightly focused spot size on the device, the He-Ne laser beam is directed to a beam expander and then focused through a microscope objective (50×, NA=0.5) with optical window correction. This gives a spot size of ~1μm on the sample. To minimize laser heating, we limit the laser power on the device to be below ~700μW. Such laser power levels give good interferometric signals in resonance measurements, and do not induce observable frequency shift due to parasitic laser heating.

Optimizing the alignment of the optics is crucial for our measurements because of the minimal motions of the devices due to thermomechanical fluctuations. Position of the measured device is adjusted using a motorized stage (Prior Scientific ProScan III). The MoS<sub>2</sub> diaphragm's motion with respect to the underneath Si surface changes the interference and therefore leads to small-signal variations in the interferometric intensity. This is then detected with a low-noise photodetector (PD) (New Focus 1801), and recorded by an RF/microwave spectrum analyzer (Agilent E4440A). Most of the measurements are performed under moderate vacuum (~6mTorr) except for the pressure dependence measurements.

## S1.2. Interferometric Motion Transduction

The reflectance  $R$  of the device (total reflected light intensity divided by incidence light intensity) is determined by the interference of the reflected light from all the interfaces. Analysis of the multiple reflections inside the device structure (Fig. S2 inset) gives<sup>1</sup>

$$\frac{I_{\text{interferometry}}}{I_{\text{incident}}} = \left| \frac{r_1 e^{i(\phi_1 + \phi_2)} + r_2 e^{-i(\phi_1 - \phi_2)} + r_3 e^{-i(\phi_1 + \phi_2)} + r_1 r_2 r_3 e^{i(\phi_1 - \phi_2)}}{e^{i(\phi_1 + \phi_2)} + r_1 r_2 e^{-i(\phi_1 - \phi_2)} + r_1 r_3 e^{-i(\phi_1 + \phi_2)} + r_2 r_3 e^{i(\phi_1 - \phi_2)}} \right|^2. \quad (\text{S1})$$

Here,  $r_1$ ,  $r_2$  and  $r_3$  are reflection coefficients at the vacuum-MoS<sub>2</sub>, MoS<sub>2</sub>-vacuum, and vacuum-Si interface:

$$r_1 = \frac{n_{\text{vacuum}} - n_{\text{MoS}_2}}{n_{\text{vacuum}} + n_{\text{MoS}_2}}, \quad r_2 = \frac{n_{\text{MoS}_2} - n_{\text{vacuum}}}{n_{\text{MoS}_2} + n_{\text{vacuum}}}, \quad r_3 = \frac{n_{\text{vacuum}} - n_{\text{Si}}}{n_{\text{vacuum}} + n_{\text{Si}}}; \quad (\text{S2})$$

and  $\phi_1$ ,  $\phi_2$  are the corresponding phase shifts:

$$\phi_1 = \frac{2\pi n_{\text{MoS}_2} d_1}{\lambda}, \quad \phi_2 = \frac{2\pi n_{\text{vacuum}} d_2}{\lambda}, \quad (\text{S3})$$

where  $d_1$  is the MoS<sub>2</sub> thickness,  $d_2$  is the vacuum gap depth, and  $\lambda$  is the laser wavelength.

Using Eqs. S1-S3, the reflectance  $R$ 's dependence on vacuum gap depth is calculated and plotted in Fig. S3 for  $\lambda=632.8\text{nm}$  and  $d_1=21\text{nm}$ , as an example. We use  $n_{\text{vacuum}}=1$ ,  $n_{\text{MoS}_2}=5.263-1.140i$  and  $n_{\text{Si}}=3.881-0.019i$ . The dependence of  $R$  on  $d_1$  is discussed in Section S1.5.

With no external drive, thermomechanical (Brownian) motions of the device lead to fluctuations of the vacuum gap size  $d_2$ . These spatial fluctuations are transduced into the variations in  $R$ . Therefore, the slope at  $d_2=290\text{nm}$  (the SiO<sub>2</sub> thickness) in Fig. S2 determines the ‘‘displacement-to-optical-reflectance’’ responsivity, and is estimated to be  $-0.38\%/nm$ .

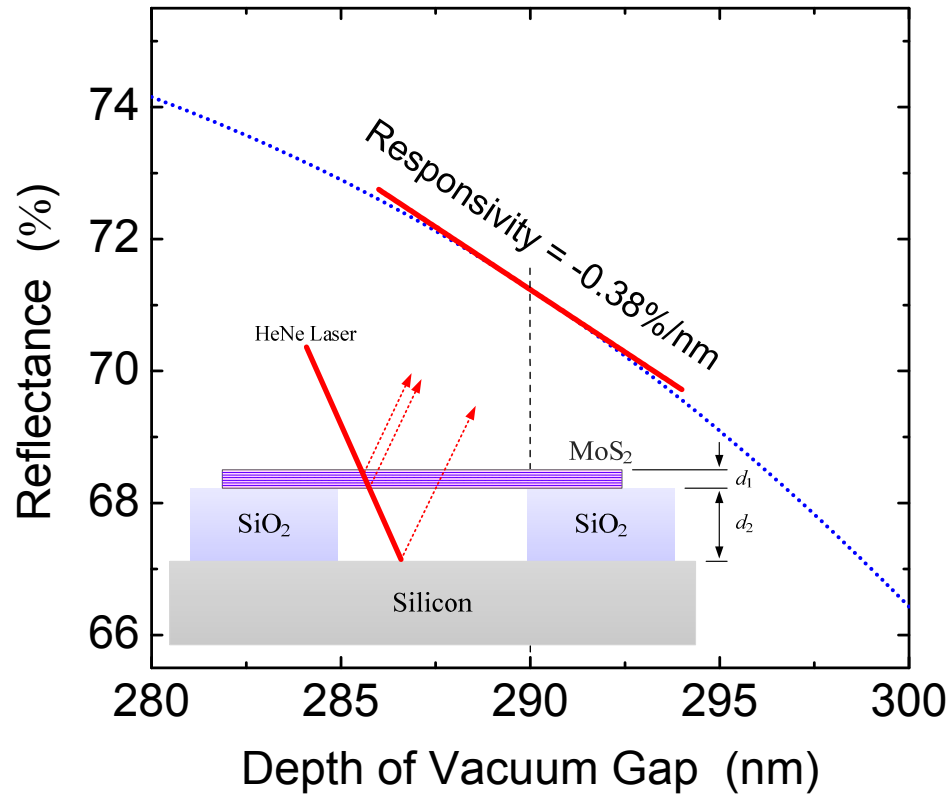


**Figure S2. Optical reflectance of the device versus the vacuum gap size for  $\lambda=632.8\text{nm}$  and  $d_1=21\text{nm}$ .** The slope of the curve at 290nm (the vacuum gap size in our devices, indicated by the vertical dashed line) determines the responsivity of the system. *Inset:* Schematic of reflection at multiple interfaces. (Higher order reflections are not shown for clarity, but are included in the calculation).

### ***S1.3. Thermomechanical Resonance Measurement and Noise Analysis***

The signal measured on the spectrum analyzer typically takes the form of a resonance response on top of a frequency-dependent background (see Fig. S3, and also Fig. 1 and Fig. 2 in the main text for typical examples). To relate the measured electronic signal to the mechanical motion of the device, we perform analysis on the thermomechanical noise.

In the frequency domain, the thermomechanical motion of a resonator is given as<sup>3</sup>

$$S_{x,th}^{1/2}(\omega) = \left[ \frac{4\omega_0 k_B T}{QM_{eff}} \cdot \frac{1}{(\omega_0^2 - \omega^2)^2 + (\omega_0 \omega / Q)^2} \right]^{\frac{1}{2}}, \quad (S4)$$

and when the device is on resonance, the expression simplifies to

$$S_{x,th}^{1/2}(\omega_0) = \sqrt{\frac{4k_B T Q}{\omega_0^3 M_{eff}}}. \quad (S5)$$

Here,  $k_B$ ,  $T$ ,  $\omega_0$ ,  $Q$ , and  $M_{eff}$  are, respectively, the Boltzmann's constant, temperature, angular resonance frequency, quality factor, and the effective mass of the device (more details in Section S1.4). For example, for the 68.1nm-thick MoS<sub>2</sub> resonator in Fig. 1 left panel in the main text, using its dimensions, measured resonance frequency, measured  $Q$ , temperature (300K), and Eq. S5, we determine its thermomechanical displacement noise spectral density on resonance to be  $S_{x,th}^{1/2} = 125.3 \text{ fm/Hz}^{1/2}$ .

Assume the noise processes are uncorrelated, the total noise power spectral density (PSD) is the sum of the PSDs from individual noise processes. Thus we have  $S_{v,total}^{1/2} = (S_{v,th} + S_{v,sys})^{1/2}$ .

Here  $S_{v,th}^{1/2}$  is the thermomechanical motion noise spectral density translated into the electronic domain, through the ‘displacement-to-voltage’ responsivity  $\mathfrak{R} \equiv S_{v,th}^{1/2}/S_{x,th}^{1/2}$ . The other term,  $S_{v,sys}^{1/2}$ , is the voltage noise floor of the measurement system, which depends on the details of the detection scheme. Typically we have  $S_{v,sys}^{1/2} \approx 0.1\text{--}0.35\mu\text{V/Hz}^{1/2}$  in the 10–60MHz frequency band, which slightly increases with increasing frequency. The level of  $S_{v,sys}^{1/2}$  determines the off-resonance ‘baseline’ background ( $S_{v,total}^{1/2} \approx S_{v,sys}^{1/2}$  off the resonance).

We fit our data to the expression for  $S_{v,total}^{1/2}$ , by using  $S_{v,th}^{1/2} = \mathfrak{R} \times S_{x,th}^{1/2}$  and treating  $S_{v,sys}^{1/2}$  as a frequency-dependent function:

$$S_{v,total}^{1/2} = \left( \mathfrak{R}^2 \times S_{x,th} + S_{v,sys} \right)^{1/2} = \sqrt{\mathfrak{R}^2 \left( \frac{4\omega_0 k_B T}{QM_{eff}} \cdot \frac{1}{(\omega_0^2 - \omega^2)^2 + (\omega_0 \omega / Q)^2} \right) + S_{v,sys}}. \quad (\text{S6})$$

From the fitting we obtain  $S_{v,sys}^{1/2}$ ,  $Q$ , and  $\mathfrak{R}$  (assuming  $T = 300\text{K}$ ).

Figure S3 (from the same device as in main text Fig. 1 left panel) shows an example of the fitting to the measured noise spectral density, with data (measured voltage spectral density,  $S_{v,total}^{1/2}$ ) plotted against the left y-axis. We then convert voltage spectral density to displacement spectral density through the relationship  $S_x^{1/2} = S_v^{1/2}/\mathfrak{R}$ , with displacement scale displayed on the right y-axis. The displacement sensitivity of the measurement system is defined as  $S_{x,sys}^{1/2} = S_{v,sys}^{1/2}/\mathfrak{R}$ , the equivalent ‘fictitious’ displacement that would transduce into the actual electronic-domain noise floor of the measurement system. For example, the 68.1nm-thick MoS<sub>2</sub> resonator, from which the data is shown in Fig. S3, is a motion transducer with a displacement

sensitivity of  $S_{x,sys}^{1/2} = 49.5 \text{ fm/Hz}^{1/2}$ . From the plot one can directly tell that the responsivity of this system is  $\mathfrak{R} = S_{v,sys}^{1/2} / S_{x,sys}^{1/2} = 0.117 \mu\text{V/Hz}^{1/2} / 0.0495 \text{ pm/Hz}^{1/2} = 2.36 \mu\text{V/pm}$ . We note that MoS<sub>2</sub> devices with different thicknesses have different responsivities and sensitivities (see Section S1.5 for more details). For each of the MoS<sub>2</sub> devices, we have carefully performed similar signal transduction analysis as briefly discussed above and illustrated in Fig. S3.

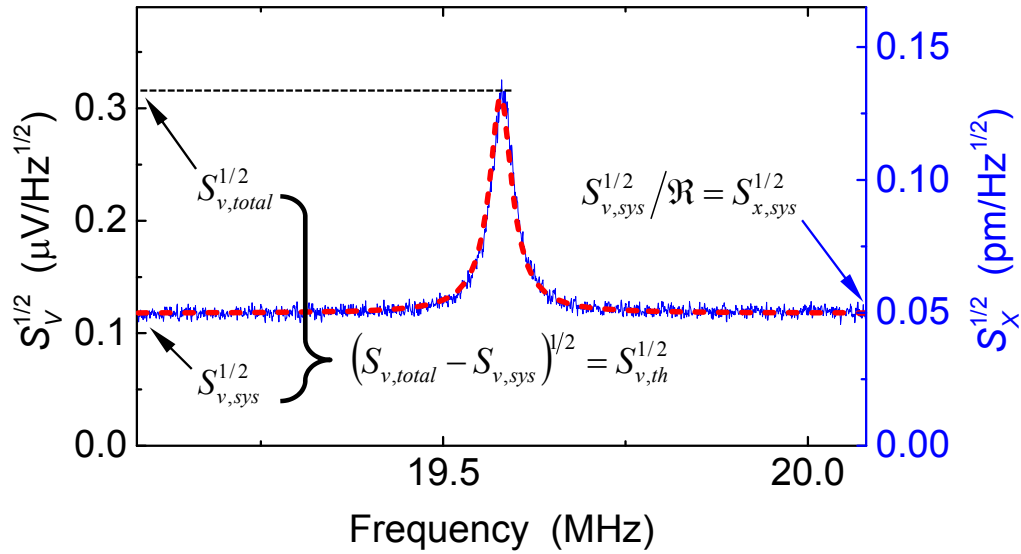


**Figure S3. Example of measured thermomechanical resonance spectrum and analysis** (from the same device as in main text Fig. 1 left panel). Annotations indicate how various quantities can be read off from the figure and are related to each other. See the text in Section S1.3 for more details.

#### ***S1.4. Calculation of the Effective Mass of the Resonator***

In order to use Eq. S4 and S5 to estimate the amplitude of the Brownian motion, one needs to calculate the effective mass of the device, which depends on the mode shape of the resonance. Here we calculate the effective masses for a circular plate and a membrane in their fundamental flexural modes of out-of-plane vibrations. For a circular plate with clamped edge, the deflection for the lowest mode ( $m=0, n=1$ ) as a function of the normalized radial position  $r$  ( $0 \leq r \leq 1$ ) is given as<sup>4</sup>

$$Z_{01}(r) = J_0(\beta_{01} \cdot r) - \frac{J_0(\beta_{01})}{I_0(\beta_{01})} \cdot I_0(\beta_{01} \cdot r), \quad (\text{S7})$$

where  $J_0$  is the 0<sup>th</sup>-order Bessel function  $J$ , and  $I_0$  is the 0<sup>th</sup>-order extended Bessel function  $I$ . For the fundamental mode,  $\beta_{01}^2 = 10.216$ . The normalized modal shape is defined as

$$u_{01}(r) = \frac{Z_{01}(r)}{\max(Z_{01})}, \quad (\text{S8})$$

and the effective mass can be calculated as

$$M_{eff,01} = M \cdot \frac{1}{\pi} \int_0^1 2\pi r \cdot [u_{01}(r)]^2 dr. \quad (\text{S9})$$

Here  $M$  is the total mass of the resonator. Using Eq. S9 we calculate the effective mass of a circular plate to be  $M_{eff,01} = 0.1828M$  for the fundamental out-of-plane mode.

Similarly, for a circular membrane, the mode shape is

$$Z_{01}(r) = J_0(\beta_{01} \cdot r), \quad (\text{S10})$$

where  $\beta_{01} = 2.405$ . This yields an effective mass of  $M_{eff,01} = 0.2695M$ .

### ***S1.5. Effect of Device Thickness***

We examine how the MoS<sub>2</sub> thickness affects the interferometry measurement. Using the same equations in section S1.2 (Eqs. S1-S3), the dependence of the device reflectance  $R$  on MoS<sub>2</sub> thickness is calculated and plotted in Fig. S4, illustrating how the “displacement-to-optical-reflectance” responsivity is modulated by the device thickness  $d_1$ .

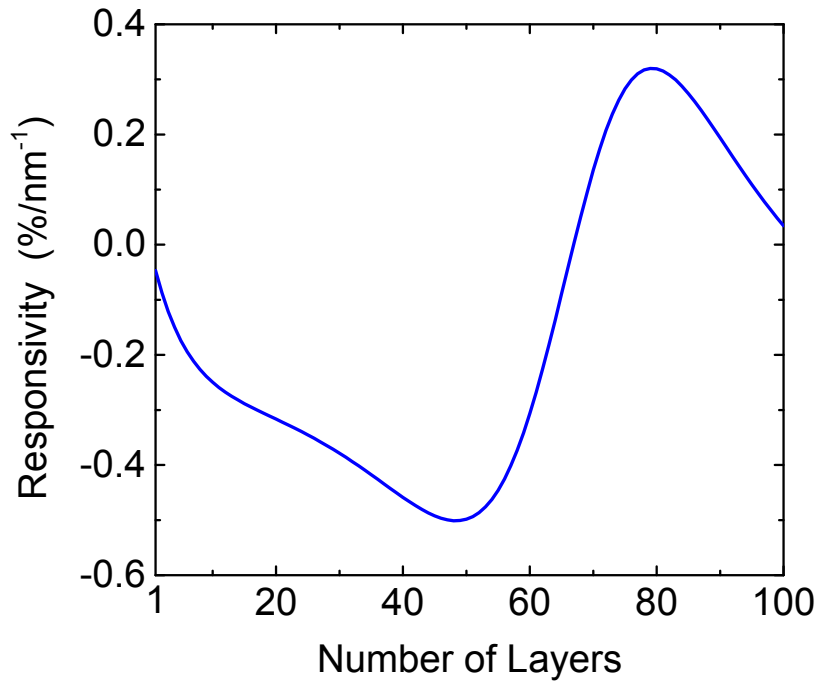


**Figure S4. Calculated optical interferometric transduction responsivity as a function of MoS<sub>2</sub> thickness.** Note that for certain thickness, the responsivity is 0.

## S2. AFM and Thickness Measurement

We obtain AFM images and estimate thicknesses of our devices using an Agilent N9610A AFM. We start with coarse scans to locate the device and center it in the scan field, followed by slow scans with high resolution over the entire device area. We then take multiple traces across the edge of the flake in the resulting AFM data, and multiple measurements are made on each trace. The average value and standard deviation of the measured height differences are used as values for the thickness and its uncertainty. Figure S5 shows the AFM data from one of our thinnest devices (resonance shown in Fig. 2b of the main text).

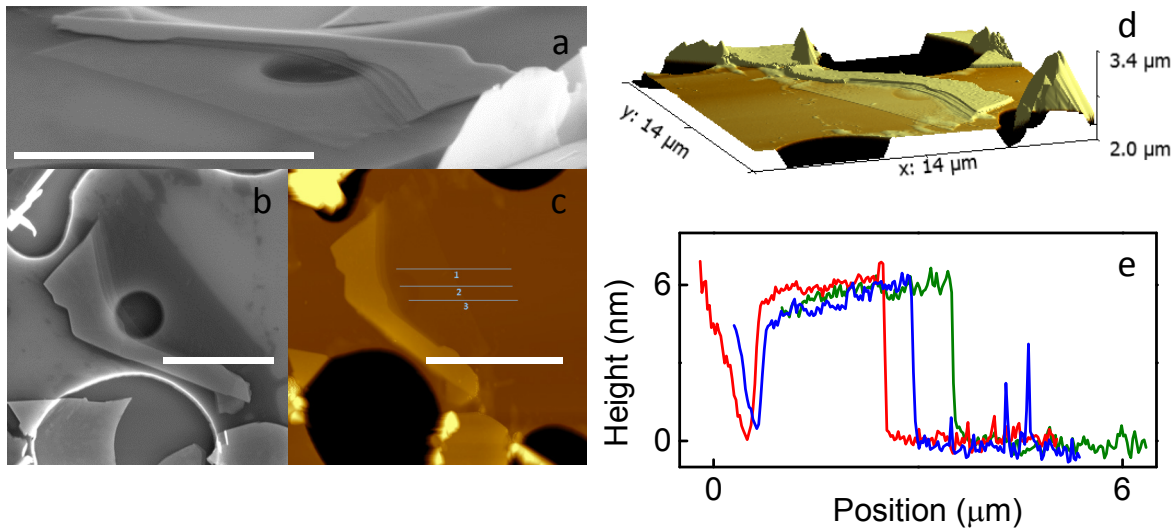


**Figure S5. AFM and thickness measurement of our thinnest device ( $t=6.1\pm 0.2\text{nm}$ ).** **a, b:** Perspective view and top view SEM images. **c:** AFM scan with lines indicating the position of the height traces. **d:** 3D AFM image. **e:** the height traces from the AFM scan. The green, blue and red lines correspond to trace 1, 2 and 3 in **c**, respectively. All scale bars:  $5\mu\text{m}$ .

### S3. Theoretical Analysis of Device Elastic Behavior and Frequency Scaling

This section presents our theoretical analysis and modeling of the resonance frequency. For a circular disk with bending rigidity and non-zero tension, the resonance frequency is<sup>5,6</sup>

$$\omega_{mn} = \left( k_2^{mn} \frac{d}{2} \right) \sqrt{\frac{16D}{\rho d^4} \left[ \left( k_2^{mn} \frac{d}{2} \right)^2 + \frac{\gamma d^2}{4D} \right]}. \quad (\text{S11})$$

Here  $\omega_{mn}$  is the angular frequency for the resonance mode  $(m, n)$ ,  $d$  is the diameter of the disk,  $\rho$  is the areal (2D) mass density (kg/m<sup>2</sup>) of the material,  $\gamma$  is the tension (force per unit length, in N/m, as in surface tension) inside the disk.  $D = E_Y t^3 / [12(1 - \nu^2)]$  is the bending rigidity, with  $E_Y$  being the Young's modulus,  $t$  the thickness of the disk, and  $\nu$  the Poisson's ratio.  $k_2^{mn}$  is a mode-dependent parameter that is usually solved numerically.

In the limit of an ideal membrane in which tension dominates,  $\gamma d^2 / D \rightarrow \infty$ , Eq. S11 becomes

$$\omega_{mn} = \frac{(k_2^{mn} d)}{d} \sqrt{\frac{\gamma}{\rho}}, \quad (\text{S12})$$

which is the 'membrane limit' of resonance frequency dependence on geometry. Note that the formality of this equation may differ from the other forms of membrane equation, because we used surface tension  $\gamma$  (force per unit length, N/m), which is more meaningful for 2D structures, instead of other forms such as tension (force, in N) or stress (force per unit cross-sectional area, with units of Pa, N/m<sup>2</sup>) which are more applicable to 3D structures. As a result, the frequency depends on the thickness  $t$  through the dependence on  $\rho$ , the 2D mass density.

In the other limit where the bending rigidity dominates,  $\gamma d^2 / D \rightarrow 0$ , Eq. S11 approaches

$$\omega_{mn} = \frac{(k_2^{mn} d)^2}{d^2} \sqrt{\frac{D}{\rho}}, \quad (\text{S13})$$

which is the well-known equation for an ideal circular plate. Both limits are plotted as dashed lines in Fig. 4 of the main text.

In the regime where *neither* tension *nor* bending rigidity is negligible,  $(k_2^{mn} d/2)$  can be approximated by the following analytical expression<sup>6</sup>

$$(k_2^{mn} d/2) = \alpha + (\beta - \alpha) e^{[-\eta e^{\delta \ln(x)}]}, \quad (\text{S14})$$

where  $x = \gamma d^2 / (4D)$ . For the fundamental-mode ( $m=0, n=1$ ) resonance, the values of parameters  $\alpha$ ,  $\beta$ ,  $\eta$ ,  $\delta$  are given in Ref. 6. It is also shown that the error between the numerical solution and the analytical approximation remains below 3.8% for this mode<sup>6</sup>.

Using this analytical approximation, we compute the fundamental-mode resonance frequency of clamped MoS<sub>2</sub> diaphragms with different diameters and thicknesses (see Fig. 4 main text). Here we use 5.06g/cm<sup>3</sup> for the 3D mass density of MoS<sub>2</sub>, and 0.7nm as the monolayer thickness<sup>7,8</sup>. Poisson's ratio is chosen to be  $\nu = 0.165$ , same as that of graphite in the basal plane<sup>9</sup>. Indeed, our results are not sensitive to the value of Poisson's ratio within a reasonable range: when a device is near the ideal membrane limit, Poisson's ratio has no effect on the resonance as it does not appear in the membrane equation; when it is in the plate limit, Poisson's ratio enter the equation through the bending rigidity  $D$ ,

$$\omega_{mn} \propto \sqrt{D} \propto \sqrt{\frac{1}{(1-\nu^2)}}. \quad (\text{S15})$$

If we use some other values from the literature, such as  $0.25^{10}$ ,  $0.125^{11}$ , or  $0.27^{12}$ , the resulting difference is always less than 2.5%.

We use Young's modulus of  $E_Y=0.2\text{TPa}$  as suggested by existing works<sup>11,13,14,15,16</sup>. The calculated results are consistent with our experimental data. In Fig. 4 of the main text, we show calculation for tension values ranging from 0.1–0.5N/m (except for  $d=0.5\mu\text{m}$ ), as typically observed in exfoliated nanosheets<sup>13,14,15,17</sup>. For the  $0.5\mu\text{m}$  devices, we show an additional curve with a tension of 4.2N/m, which can lead to GHz  $\text{MoS}_2$  resonators. This tension level corresponds to a strain of only 3% in monolayer and 1.5% in bilayer, still significantly below the intrinsic strain limit of this material<sup>13,16</sup>.

#### **S4. Measuring Device Temperature and Laser Heating Effect**

Experimentally determining the temperature of a suspended  $\text{MoS}_2$  device is particularly challenging, given the small dimensions and the configurations of our devices (*e.g.*, no electrical contacts or electrodes). Conventional thermometry techniques are not applicable. In this work, we exploit intrinsic properties of our devices and use the device itself as a thermometer. The specific technique we employ, called noise thermometry,<sup>3,18,19,20</sup> uses the device's intrinsic thermomechanical noise spectrum to precisely determine its temperature, according to the fundamental equipartition theorem and statistical mechanics. This allows us to directly measure the device temperature with very good precision, through analyzing the noise spectrum of the device's thermomechanical motion, at a series of laser power levels. The device temperature is related to its thermomechanical motion amplitude by

$$T = \frac{k_{eff}}{2\pi k_B} \int_0^\infty S_{x,th}(\omega) d\omega. \quad (\text{S16})$$

Here,  $k_{eff}$  is the effective spring constant of the resonator and  $k_B$  is the Boltzmann's constant. To use the measured voltage domain spectrum density, we use  $S_{v,th}^{1/2} = \Re \times S_{x,th}^{1/2}$  (see Section S1.3):

$$T = \frac{k_{eff}}{2\pi k_B} \int_0^\infty \left( \frac{S_{v,th}^{1/2}(\omega)}{\Re} \right)^2 d\omega, \quad (\text{S17})$$

where  $\Re$  is responsivity (displacement-to-voltage transduction gain) of the measurement setup, and can be calibrated experimentally.<sup>21</sup>

To examine the heating effects, we use different laser powers. Since  $\Re$  linearly depends on the incident laser power, we normalize our expression accordingly:

$$T = C \frac{k_{eff}}{2\pi k_B} \int_0^\infty \left( \frac{S_{v,th}^{1/2}(\omega)}{I} \right)^2 d\omega, \quad (\text{S18})$$

where  $I$  is the incident laser power and  $C$  is a constant which remains the same for all laser power levels.

At very low incident laser power levels ( $\sim 100\mu\text{W}$  to  $\sim 700\mu\text{W}$ ), we repeatedly observe that the resonance characteristics (center frequency  $f_0$  and  $Q$ ) are stable and relatively constant (while we observe frequency shift at higher laser power levels). Our noise thermometry confirms that at these low laser power levels, the device temperature is near room temperature ( $\sim 300\text{K}$ ). Figure S6 plots the temperature measured from thermomechanical noise thermometry using Eqs. S16-S18 for two different devices, demonstrating negligible laser heating effect when the incident laser power is below  $\sim 700\mu\text{W}$ .

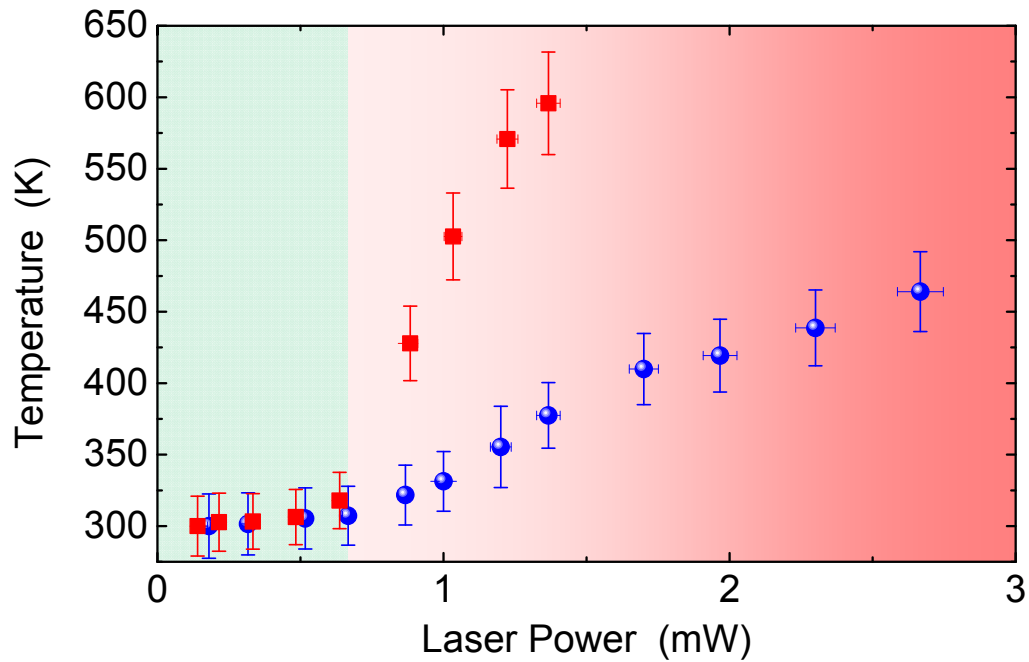


**Figure S6. Measured device temperature under different levels of incident laser power.** Data shown here have been taken from two different MoS<sub>2</sub> resonators. The green color zone indicates the region with negligible laser heating effect. Beyond this calibration, we have performed our resonance measurements for all the devices with laser power levels in the green zone.

### S5. Measurement of Pressure Dependence

Most of the thermomechanical resonance measurements have been performed in moderate vacuum. In some similar structures made with graphene, bulging due to pressure difference caused by trapped air in the cavity has been observed<sup>22</sup>. We examine such effect in our MoS<sub>2</sub> device with SEM/AFM and resonance measurements.

In edge-clamped circular membrane with different pressure on different sides, the maximum deflection at the center is related to the pressure difference by<sup>23</sup>

$$\Delta p = \frac{4tW_0}{a^2} \left( \frac{4}{3} \frac{t^2}{a^2} \frac{E_Y}{1-\nu^2} + \frac{\gamma}{t} + \frac{64}{105} \frac{W_0^2}{a^2} \frac{E_Y}{1-\nu^2} \right) \quad (\text{S19})$$

where  $\Delta p$  is the pressure difference,  $t$  is the thickness,  $\gamma$  is the initial tension (in N/m) in the membrane,  $a$  is the radius,  $E_Y$  is Young's modulus,  $\nu$  is Poisson's ratio, and  $W_0$  is the deflection of membrane. Using our thinnest 1.9 $\mu\text{m}$ -diameter device (#20 in Table S1) as an example, we estimate the deflection under  $\Delta p = 10^5 \text{ Pa}$  (using  $\gamma = 0.3 \text{ N/m}$ ) is 25nm. From both SEM and AFM measurements we do not observe clear evidence confirming such bulging effect (Fig. S5). We have found the same behavior for all the devices we measured.

Furthermore, we have performed pressure dependence measurement on the thermomechanical resonances. If there were air volume trapped underneath the MoS<sub>2</sub> diaphragm, as the external pressure in the vacuum chamber goes down, we would have expected to observe the resonance frequency increases due to increasing tension induced by the growing pressure difference (Fig. S7, magenta dashed line), as seen in some graphene resonators with similar geometry<sup>18</sup>. However, we have not observed this trend in the measured resonance frequency of our devices based on MoS<sub>2</sub> diaphragms fully covering the microtrenches. Measured data from one such example is shown in Fig. S7 (blue circles in the middle). As shown, these devices behave the same way as the devices based on MoS<sub>2</sub> diaphragms incompletely covering the circular microtrench (data from an example device is shown in Fig. S7, red half-filled circles in the bottom), which should not experience any pressure difference. These results indicate that our MoS<sub>2</sub> resonators possibly do not experience any bulging and tensioning induced by sustained trapped air underneath the MoS<sub>2</sub> diaphragms.

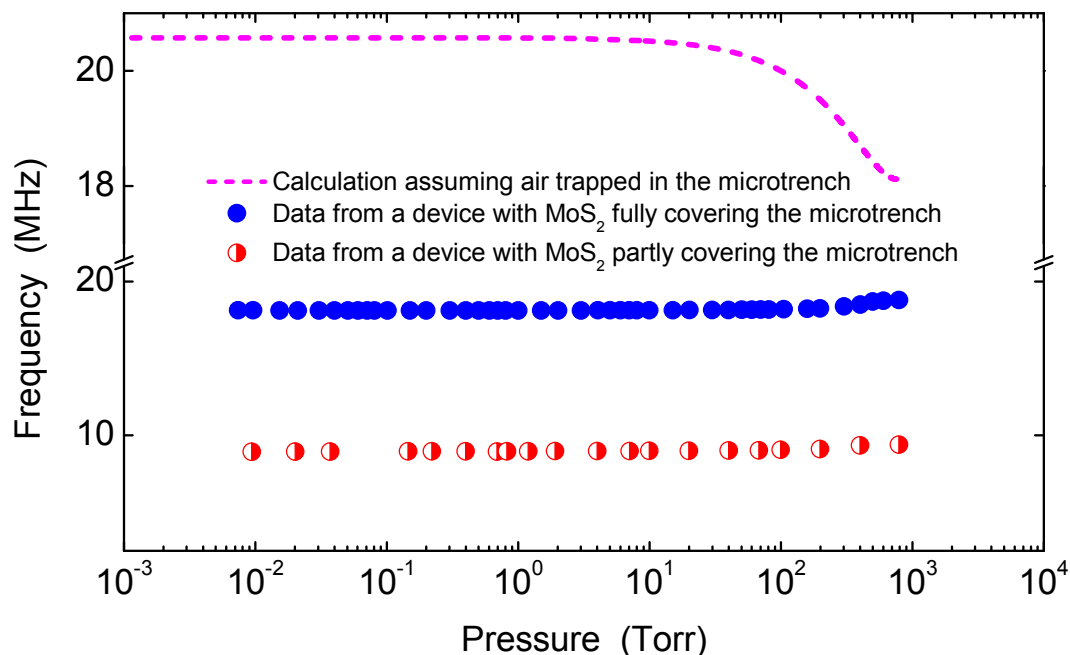


**Figure S7. Measured pressure dependence of resonance frequency.** *Dashed line:* theoretical calculation of the resonance frequency of a MoS<sub>2</sub> resonator with 1atm of air trapped underneath the MoS<sub>2</sub> diaphragm (using geometry from device #2 in Table S1). Note the curve is plotted on a separate scale than the experimental data for clarity. *Blue circles:* measured resonance frequency of such a device (#2 in Table S1). *Red half-filled circles:* measured data from a device where MoS<sub>2</sub> diaphragm partially covers the microtrench.

## S6. List of All Devices and Their Parameters

Figure S8 reproduces Fig. 3a&b in the main text. Table S1 provides a list all the devices we have measured, with their specifications and parameters. Each device in Fig. S8 is indexed and labeled with a number, corresponding to the device number listed in Table S1.

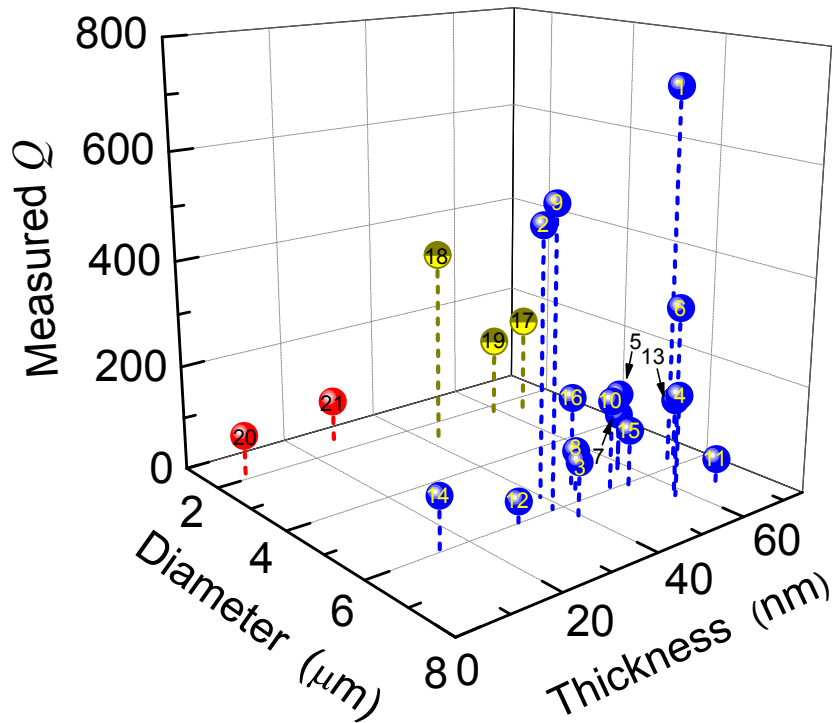
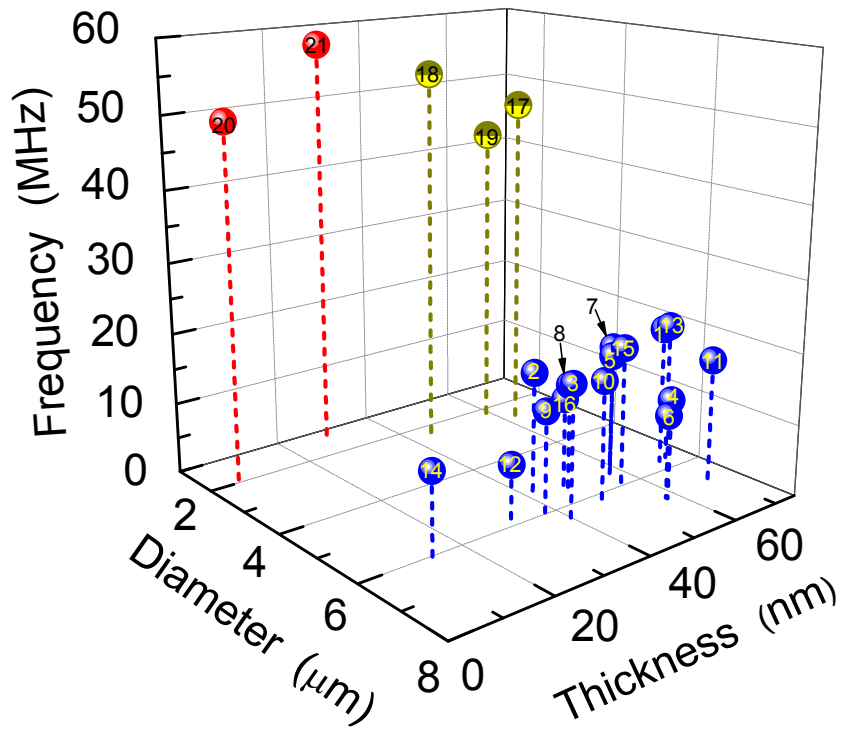


**Figure S8.** Measured resonance frequency and quality ( $Q$ ) factors of all the devices. (These plots are reproductions of those in Fig. 3a&b in the main text, with all devices labeled).

**Table S1 | List of Devices and Their Parameters**

Device #	Diameter $d$ ( $\mu\text{m}$ )	Thickness $t$ (nm)	Resonance Frequency $f_0$ (MHz)	Quality Factor $Q$	$f_0 \times Q$ (MHz)	Displacement Sensitivity $S_{x,\text{sys}}^{1/2}$ (fm/Hz <sup>1/2</sup> )	Comments
1	5.71	68.1±0.8	19.68	710	13900	49.5	Fig. 1, Left Panel
2	5.51	39.6±0.5	17.99	500	8995	91.7	
3	6.38	39.6±0.5	26.85	100	2685	171.9	
4	6.81	57.5±2.1	14.06	190	2671	30.2	
5	5.53	57.5±2.1	17.25	150	2588	39.9	
6	6.78	57.5±2.1	11.72	350	4102	31.4	
7	5.53	57.5±2.1	18.46	110	2031	32.2	
8	5.73	45.4±1.1	15.74	80	1259	84.9	
9	5.96	38.0±1.6	14.13	550	7772	33.5	Fig. 1, Right Panel
10	6.17	48.8±1.1	16.76	180	3017	90.8	
11	6.93	66.0±1.1	18.29	50	914.5	51.0	
12	5.99	30.3±0.3	8.49	40	340	41.4	
13	5.65	70.2±0.7	19.65	110	2162	43.6	
14	6.06	13.6±0.8	11.54	105	1212	99.4	
15	6.05	54.6±2.5	19.99	105	2099	69.5	
16	5.51	46.6±1.3	12.99	170	2208	41.3	
17*	2.69	62.2±0.7	48.10	200	9620	51.1	Fig. 2a
18*	2.41	57.5±2.1	43.77	160	7003	40.9	
19*	2.53	43.0±1.4	53.72	370	19880	49.5	Fig. 2c
20	1.90	6.1±0.7	49.70	80	4473	243.1	Fig. 2b
21	1.51	27.2±0.5	57.89	80	4921	205.1	Fig. 2d

\*Device with less than complete coverage.

## References

---

- <sup>1</sup> Blake, P., Hill, E.W., Castro Neto, A.H., Novoselov, K.S., Jiang, D., Yang, R., Booth, T.J. & Geim, A.K. Making Graphene Visible. *Appl. Phys. Lett.* **91**, 063124 (2007).
- <sup>2</sup> Beal, A.R. & Hughes, H.P. Kramers-Krönig Analysis of the Reflectivity Spectra of 2H-MoS<sub>2</sub>, 2H- MoSe<sub>2</sub> and 2H-MoTe<sub>2</sub>. *J. Phys. C: Solid State Phys.* **12**, 881-890 (1979).
- <sup>3</sup> Cleland, A.N. *Foundations of Nanomechanics: from Solid-State Theory to Device Applications*. Springer, New York, 2003.
- <sup>4</sup> Graff, K.F. *Wave Motion in Elastic Solids*. Dover Publications, New York, 1991.
- <sup>5</sup> Wah, T. Vibration of Circular Plates. *J. Acoust. Soc. Am.* **34**, 275-281 (1962).
- <sup>6</sup> Suzuki, H., Yamaguchi, N. & Izumi, H. Theoretical and Experimental Studies on the Resonance Frequencies of a Stretched Circular Plate: Application to Japanese Drum Diaphragms. *Acoust. Sci. Technol.* **30**, 348–354 (2009).
- <sup>7</sup> Mak, K.F., Lee, C., Hone, J., Shan, J. & Heinz, T.F. Atomically Thin MoS<sub>2</sub>: A New Direct-Gap Semiconductor. *Phys. Rev. Lett.* **105**, 136805 (2010).
- <sup>8</sup> Splendiani, A., Sun, L., Zhang Y., Li T., Kim, J., Chim, C.-Y., Galli, G. & Wang, F. Emerging Photoluminescence in Monolayer MoS<sub>2</sub>. *Nano Lett.* **10**, 1271-1275 (2010).
- <sup>9</sup> Blakslee, O.L., Proctor, D.G., Seldin, E.J., Spence, G.B. & Weng, T. Elastic Constants of Compression-Annealed Pyrolytic Graphite. *J. Appl. Phys.* **41**, 3373-3382 (1970).
- <sup>10</sup> Yue, Q., Kang, J., Shao, Z., Zhang, X., Chang, S., Wang, G., Qin, S. & Li, J. Mechanical and Electronic Properties of Monolayer MoS<sub>2</sub> under Elastic Strain. *Phys. Lett. A* **376**, 1166-1170 (2012).
- <sup>11</sup> Lovell, M.R., Khonsari, M.M. & Marangoni, R.D. A Finite Element Analysis of the Frictional Forces between a Cylindrical Bearing Element and MoS<sub>2</sub> Coated and Uncoated Surfaces. *Wear* **194**, 60-70 (1996).
- <sup>12</sup> Feldman, J.L. Elastic Constants of 2H-MoS<sub>2</sub> and 2H-NbSe<sub>2</sub> Extracted from Measured Dispersion Curves and Linear Compressibilities. *J. Phys. Chem. Solids* **37**, 1141-1144 (1976).

- 
- <sup>13</sup> Bertolazzi, S., Brivio, J. & Kis, A. Stretching and Breaking of Ultrathin MoS<sub>2</sub>. *ACS Nano* **5**, 9703-9709 (2011).
- <sup>14</sup> Castellanos-Gomez, A., Poot M., Steele, G.A, van der Zant, H.S.J., Agraït, N. & Rubio-Bollinger, G. Mechanical Properties of Freely Suspended Semiconducting Graphene-Like Layers Based on MoS<sub>2</sub>. *Nanoscale Res. Lett.* **7**, 233 (2012).
- <sup>15</sup> Castellanos-Gomez, A., Poot M., Steele, G.A, van der Zant, H.S.J., Agraït, N. & Rubio-Bollinger, G. Elastic Properties of Freely Suspended MoS<sub>2</sub> Nanosheets. *Adv. Mater.* **24**, 772-775 (2012).
- <sup>16</sup> Li, T. Ideal Strength and Phonon Instability in Single-Layer MoS<sub>2</sub>. *Phys. Rev. B* **85**, 235407 (2012).
- <sup>17</sup> Lee, C., Wei, X., Kysar, J. W. & Hone, J. Measurement of the Elastic Properties and Intrinsic Strength of Monolayer Graphene. *Science* **321**, 385-388 (2008).
- <sup>18</sup> Bleszynski-Jayich, A.C., Shanks, W.E. & Harris, J.G.E. Noise Thermometry and Electron Thermometry of a Sample-on-Cantilever System below 1 Kelvin. *Appl. Phys. Lett.* **92**, 013123 (2008).
- <sup>19</sup> Montinaro, M., Mehlin, A., Solanki, H.S., Peddibhotla, P., Mack, S. & Awschalom, D.D. Feedback Cooling of Cantilever Motion Using a Quantum Point Contact Transducer. *Appl. Phys. Lett.* **101**, 133104 (2012).
- <sup>20</sup> Poggio, M., Degen, C.L., Mamin, H.J. & Rugar, D. Feedback Cooling of a Cantilever's Fundamental Mode below 5 mK. *Phys. Rev. Lett.* **99**, 017201 (2007).
- <sup>21</sup> Hiebert, W.K., Vick, D., Sauer, V. & Freeman, M.R. Optical Interferometric Displacement Calibration and Thermomechanical Noise Detection in Bulk Focused Ion Beam-Fabricated Nanoelectromechanical Systems. *J. Micromech. Microeng.* **20**, 115038 (2010).
- <sup>22</sup> Bunch, J.S., Verbridge, S.S., Alden, J.S., van der Zande, A.M., Parpia, J.M., Craighead, H.G. & McEuen, P.L. Impermeable Atomic Membranes from Graphene Sheets. *Nano Lett.* **8**, 2458-2462 (2008).
- <sup>23</sup> Schomburg, W. K. *Introduction to Microsystem Design*. Springer, 2011.